Robust Ballistic Catching: A Hybrid System Stabilization Problem

Markus M. Schill ⬤ and Martin Buss ⬤

Abstract—This paper addresses a remaining gap between today's academic catching robots and their future in industrial applications: reliable task execution. A novel parameterization is derived to reduce the three-dimensional (3-D) catching problem to 1-D on the ballistic flight path. Vice versa, an efficient dynamical system formulation allows reconstruction of solutions from 1-D to 3-D. Hence, the body of the work in hybrid dynamical systems theory, in particular on the 1-D bouncing ball problem, becomes available for robotic catching. Uniform Zeno asymptotic stability from bouncing ball literature is adapted, as an example, and extended to fit the catching problem. A quantitative stability measure and the importance of the initial relative state between the object and end-effector are discussed. As a result, constrained dynamic optimization maximizes convergence speed while satisfying all kinematic and dynamic limits. Thus, for the first time, a quantitative success-oriented comparison of catching motions becomes available. The feasible and optimal solution is then validated on two symmetric robots autonomously playing throw and catch.

Index Terms—Catching, contact modeling, dexterous manipulation, manipulation planning, nonprehensile manipulation.

I. INTRODUCTION

ROBOTS catching an object is a challenging and frequently considered testbed to demonstrate the performance of object tracking combined with motion planning in highly dynamic environments. A successful catch relies on good solutions in both tracking and planning. Vice versa, a failed attempt is typically explained with shortcomings of the proposed solutions, e.g., neglected dynamic feasibility or inaccurate estimation of the object state. The complexity of many proposed systems hinders an analytic derivation of the mixture of errors that lead to the observed failures. This paper presents a novel and provably
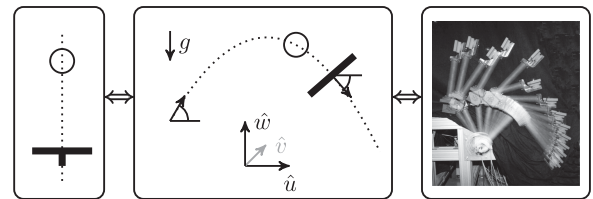
Fig. 1. Dynamical system parameterization enables ballistic nonprehensile catching with dynamically feasible offline motions using hybrid bouncing ball formalisms.

robust method for robotic catching. The approach is validated in a prototypical experimental setup.

Many previous works consider *static catching* with a gripper [1]–[4], where the goal is to track and predict the object flight trajectory with high precision as quickly as possible. The remaining time is then used to move the catching robot to a reachable kinematic goal posture such that the gripper intercepts the flight path and catches the object at the right moment. This approach generates impact forces and a rebound that can cause the object to bounce off the gripper in case of uncertainties. Thus, static approaches are limited to soft, relatively light objects, or compliant end-effectors.

Dynamic catching, in which the robot adapts to the motion of the object [5]–[9], allows handling of a wider range of objects and is less sensitive to timing accuracy [10]. Without a gripper, the goal is formulated as a generic nonprehensile [11], [12] catching task based on the fundamental dynamics [13] that model continuous contact between a free flying object and the robot end-effector.

This paper isolates fundamental hybrid dynamics of the catching problem, cf., Fig. 1, applying to most robots that could catch objects robustly. Our novel approach is characterized by three main contributions.

1) Dimensionality reduction closes the gap between ballistic catching and related hybrid control theory: allows transfer of (future) progress in hybrid control theory to robotic catching.
2) Uncertainty of object states and restitution behavior included as collisions are inevitable, even for dynamic catching–dynamic catching is realized robustly.
3) A single catching motion applies for a range of objects and initial object states (no replanning): guaranteed dynamically feasible robot motions can be found offline.

Hence, for the first time, experimental success in ballistic robotic catching becomes predictable and robust. The experimental success at the end of this paper generalizes to various

robots. This generality and robustness of the proposed approach is promising for many future (industrial) applications.

A. Robotic Catching

The fundamental problem of catching is to bring a fast flying object to rest by interaction with a robot end-effector.

Interestingly, one of the first catching systems accomplishes the task *dynamically* (velocity and acceleration matching) [5], [6] and not statically. In this early work, a 4-DOF robot with a gripper closes perpendicular to the flight direction in order to avoid impact of the object with the end-effector. The dynamic approach is necessary because vision systems are still too imprecise to determine accurate arrival times. The closing of the grasping end-effector also took a considerably long time. About the same time a "mirror law" was proposed in [7] to generate the motion for a dynamic catch in combination with a well-tuned PD-controller after the initial impact. The related problem of kinematic and dynamic feasibility is not treated formally.

More recent work addresses some of the *feasibility* problems in dynamic catching. In [8], the goal definition is extended to match the acceleration of a thrown basketball. In the case of kinematically or dynamically infeasible desired robot motions, an indirect catch is introduced, which is a single controlled rebound before the actual catch. In [14], the idea of direct and indirect catching is generalized to polygonal objects. Kinematically feasible offline trajectories are generated in [10] as the basis for a linear parameter varying (LPV) approach. With the LPV system definition asymptotic convergence to the object's trajectory is shown. Dynamic feasibility is neglected, which is later made responsible for some of the failed catching attempts in the experimental evaluation.

So far, no ballistic catching approach has formally included the *inevitable appearance of impacts* that are due to uncertain knowledge of the object state. In our preliminary analysis [9], we showed in simulation and experiments that uncertain object states may lead to undesirable relative motions if pure velocity matching is pursued. A reachability analysis showed that a proper treatment of relative acceleration has the potential to perform a graspless catch on a ballistic trajectory. These results are in line with the findings of Schaal and Atkeson [13], and more recently Ronsse *et al.* [15] and Reist and D'Andrea [16], which suggest that negative acceleration has a focusing effect on manipulation with rebounds. In this paper, we formalize, for the first time, the treatment of relative acceleration in robotic catching by means of Lyapunov-based stability analysis of the fundamental hybrid system dynamics, which expresses the problem of converging to a fixed point.

B. Hybrid Bouncing Ball

Highly related to catching with rebounds is the problem of a ball bouncing on a table under a constant gravitational field. Being a generic example for a process that is partially of continuous (flow) and partially of discrete (jump) nature, the bouncing ball is not only an illustrative example, but has motivated a body of work. A commonly revisited problem is to stabilize the ball on a periodic orbit at the example of robotic juggling [7], [15]–[25]. One approach is the use of measure differential equations [21] to model and analyze this problem. Most of the juggling approaches, however, have chosen a Poincaré map approach [7], [15], [16], [20]–[22] to tackle the problem of periodic stability. All of these Poincaré map approaches model the continuous phase with the parabolic solution in the world coordinates and then analyze the implications of intermittent contacts with a (mostly periodically) moving table. Thereby, the work in [15] and [16] confirms Schaal's early observation in [19] of the significant influence of the table acceleration on the orbital stability behavior.

Today, the progress in hybrid dynamical system theory enables a unified treatment of partially continuous and partially discrete problems. An extensive overview of the hybrid dynamical system framework we use and related stability for time-invariant hybrid systems can be found in [26]. Applications of this framework on the juggling problem can be found in [23] and [24].

For the graspless robotic catching in this paper, the fundamental underlying problem of *making the ball converge* to a fixed point on the table or end-effector [27] differs from juggling. The main difference here is the occurrence of *Zeno behavior*, which is the unique ability of hybrid systems to exhibit an infinite number of discrete events in finite time. Literature on Zeno behavior often focuses on conditions for its existence [28]–[30] for general, even nonlinear, hybrid systems and how the existence correlates to asymptotic stability [31]–[33]. The generality of these approaches, however, hinders explicit calculations of Zeno limit points or the finite Zeno time for particular initial conditions. Works [34] and [35] are a great improvement toward an explicit consideration of Zeno behavior in real-world robotics. Following the work of Goebel and Teel [32], they showed general Zeno stability for a nonautonomous bouncing ball system with set-valued relative acceleration. Concentrating on the relative dynamics between constraint and ball, they derived a necessary and sufficient condition for *uniform Zeno asymptotic stability* (UZAS) in [35] by means of a ratio between the acceleration and the kinematic coefficient of restitution. The success guarantees and extensions presented in our paper build upon this ratio and the sophisticated Lyapunov function introduced for their proof.

C. System Overview and Outline

We consider a blind robot–robot throwing and catching scenario, in which each robot is capable of performing both tasks, without change of hardware or tools. On the one hand, not requiring visual feedback comes with the advantage of arbitrary scalability. Even very short distances or widely covered flight trajectories are possible. On the other hand, visual feedback can always be added to further increase flexibility and robustness.

In order to enable a focused discussion, this paper distinguishes between four general robot motion phases per throwing and catching sequence, visualized in Fig. 2.

P1) A first robot throws an object. In this paper, optimal control based motion planning maintains dynamic feasibility and ensures dynamic fixation of the object during acceleration. At nonprehensile release, a limited and repeatable uncertainty in the object state remains.
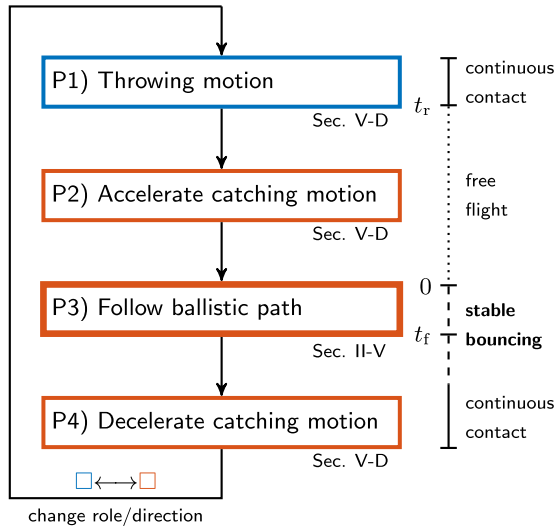
Fig. 2. Block diagram outlining the four phases for joint robot–robot throwing and catching.

Fig. 3. Distance measure h between the object surface $\mathcal{S}_O$ and end-effector surface $\mathcal{S}_E$. Rotations of the object lead to a bounded uncertainty in h for identical distances between the object center of mass and $\mathcal{S}_E$.

II. CATCHING AS 1-D PROBLEM

Here, we formulate the general problem of catching rigid, arbitrarily shaped, and fast flying objects in 3-D space. Particular attention is paid to the various uncertainties that can occur. Due to these uncertainties, at some point in the catching process, the object collides inevitably with the robot end-effector multiple times. So far, the purpose of grippers in dynamic robotic catching has been to compensate for the hardly predictable multicollision outcome. But, one could never be certain whether some of the experimental failures are still due to collisions. Therefore, we here establish a relation between the well-known bouncing ball in hybrid control theory and the robotic catching problem.

Finally, a novel parameterization is derived, which formulates the acceleration of the end-effector as input to the robotic catching system. The parameterization builds on the assumption that the object center of mass follows a ballistic trajectory. This applies for rigid objects with a sufficiently large mass-surface ratio such that the influence of aerodynamic drag is small. Hence, given a translational object state at one point in time and despite the uncertainties described in this section, the path on which the object center of mass travels is predictable and independent of shapes. A large range of parts in industrial production processes fulfills this property.

As the first main result of this paper, solutions for the 1-D hybrid bouncing ball are easily transferred back into 3-D catching. Hence, recent progress in hybrid control theory (see Section III) becomes available for robotic catching.

A. Catching Problem Formulation With Bounded Uncertainty

Consider a generalized object with surface $\mathcal{S}_O$ and a robot catching end-effector with desired catching surface $\mathcal{S}_E$ as depicted in Fig. 3. The catching surface $\mathcal{S}_E$ can be of various types, e.g., a simple plate, the palm of a gripper, or the bottom of a box as discussed later in this paper. The distance between $\mathcal{S}_O$ and $\mathcal{S}_E$ is then defined as

$$h := \min_{\boldsymbol{p}_O \in \mathcal{S}_O, \boldsymbol{p}_E \in \mathcal{S}_E} \| \boldsymbol{p}_O - \boldsymbol{p}_E \| \qquad (1)$$

where $\boldsymbol{p}_O$ and $\boldsymbol{p}_E$ are points on the object and end-effector surface, respectively. Initially, surfaces $\mathcal{S}_O$ and $\mathcal{S}_E$ are disjoint such that the object is above the end-effector. The time derivatives of h are the relative velocity $\nu := \frac{\mathrm{d}}{\mathrm{d}t} h$ and the relative acceleration

P2) A second robot accelerates from rest to the goal state, which is the initial state of P3. Again, optimal control-based motion planning is used.

P3) The second robot performs a decelerating motion on the ballistic flight path. Dynamic requirements that enable reliable ballistic catching and feasible motion planning are the major subject of this paper. Along the discussion, special attention is paid to the relative state between the object and end-effector at the start of the following motion.

P4) The second robot has to leave the ballistic flight path at some point while still in motion. Again, optimal control-based motion planning is used, but here with an inequality constraint that ensures negative relative acceleration in normal end-effector direction. Due to kinematic and dynamic limitations of typical robots, a continuous contact at the end of P3 is mostly not possible or not desirable from an efficiency (throughput) perspective.

Focusing on P3 and the transition to P4, the remainder of the paper is structured as follows. Section II starts with a generalized formulation of the catching problem. It is followed by a novel parameterization, which relates 3-D ballistic catching to the hybrid bouncing ball in 1-D. Based on boundedness of the relative acceleration, an asymptotic stability notion of the relative hybrid dynamical system is introduced in Section III and a bound on the maximal rebound height is derived. In Section IV, we discuss the predictability of catching success for spherical and arbitrarily shaped objects. In Section V, the feasibility problem is resolved with optimization-based motion planning and solutions to the individual phases are described in more detail. In order to give a better understanding of the theoretic derivations, realistic numerical examples with discussion can be found throughout the paper. Section VI presents an experimental evaluation based on the previous examples. Section VII concludes the paper.
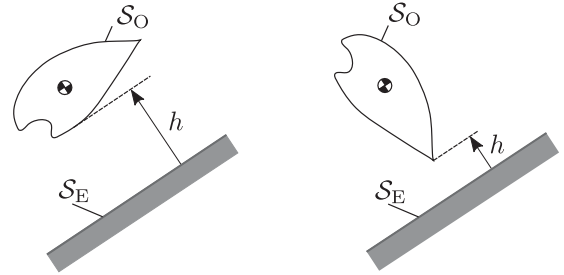
$\gamma := -\frac{d^2}{dt^2}h$. Hence, the goal of catching an arbitrarily shaped, fast flying rigid object corresponds to

$$h(t \to \infty) = 0 \quad \text{and} \quad \nu(t \to \infty) = 0 \qquad (2)$$

where $\gamma > 0$ must hold.[1] In a catching scenario, various uncertainties occur and are difficult to measure or predict. Nonetheless, boundedness can be assumed for them. The following three types will be distinguished to account for these uncertainties.

U1) Uncertainty in the initial state $h(0)$ and $\nu(0)$: e.g., due to imprecise object state estimation including orientation and rotation gained from real-time vision or based on the repeatable, open-loop robot throws as in this paper.

U2) Time-varying uncertainties in $\gamma(t)$: e.g., due to object rotation, neglected aerodynamic drag, imprecise robot motions, and object motions deviating from the ballistic path. Errors in the estimation of h and ν for $t > 0$ as a consequence of U1 lead to a translational object motion in parallel to $\mathcal{S}_E$ (perpendicular to h), which in turn affects the relative acceleration.

U3) Collisions in catching are inevitable due to U1 and U2. The outcome of such collisions is unpredictable and, thus, kinematic restitution perpendicular to $\mathcal{S}_E$ must be considered uncertain, too.

From the aforementioned problem and uncertainty formulation follows that catching an arbitrarily shaped, fast flying, rigid object is similar to stabilizing a 1-D bouncing ball with considerable uncertainties. The remainder of this paper, thus, concentrates on maximizing robustness against U1–U3 generally, instead of calculating scenario specific bounds for all the uncertainties.

B. One-dimensional Hybrid Bouncing Ball

In order to analyze the transition into continuous contact, we define relative system states $\boldsymbol{x} := [h\ \nu]^\top$ with continuous dynamics

$$\dot{\boldsymbol{x}} = \boldsymbol{f}(t, \boldsymbol{x}) := \begin{bmatrix} x_2 & -\gamma(t) \end{bmatrix}^\top. \qquad (3)$$

These continuous dynamics, however, fail to describe the entire system behavior because collisions with the end-effector surface will occur, i.e., when $h = 0$ in Fig. 3. For the collisions between the ball and end-effector in this paper, we choose the common Newtonian restitution model,[2] which is an instantaneous damped inversion of the arrival speed described by a coefficient of restitution $\rho \in [0, 1)$. Such restitution constitutes the discrete dynamics

$$\boldsymbol{x}^+ = \boldsymbol{g}(\boldsymbol{x}) := \begin{bmatrix} 0 & -\rho x_2 \end{bmatrix}^\top. \qquad (4)$$

In order to allow a combined stability analysis of the continuous and discrete dynamics, we formulate the hybrid bouncing

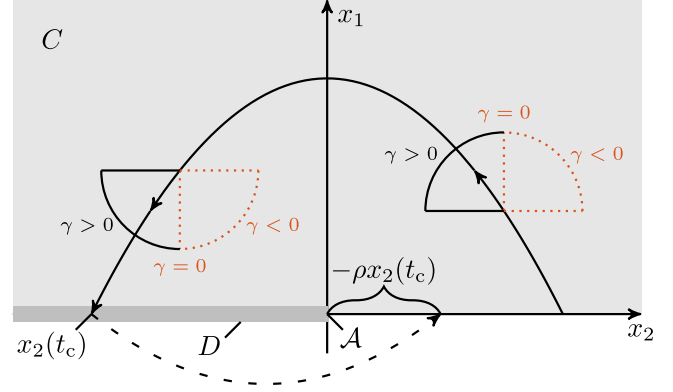Fig. 4. Flow set (5) and jump set (6) of the hybrid bouncing ball $\mathcal{H}$ with states x_1 as the height of the ball and x_2 as its velocity. The cones illustrate the influence of the γ-sign on the vector field (7) in phase space. The dashed line indicates the jump map (8).

ball dynamics $\mathcal{H} = (C, D, \boldsymbol{f}, \boldsymbol{g})$ in the form of [26] as

$$C = \{\boldsymbol{x} : x_1 \geq 0\} \qquad (5)$$

$$D = \{\boldsymbol{x} : x_1 = 0, x_2 \leq 0\} \qquad (6)$$

$$\dot{\boldsymbol{x}} = \boldsymbol{f}(t, \boldsymbol{x}) \quad \text{for all} \quad \boldsymbol{x} \in C, \ t \in [0, \infty) \qquad (7)$$

$$\boldsymbol{x}^+ = \boldsymbol{g}(\boldsymbol{x}) \quad \text{for all} \quad \boldsymbol{x} \in D \qquad (8)$$

where $(C, \boldsymbol{f})$ describe the continuous domain and dynamics (flow) and $(D, \boldsymbol{g})$ describe the discrete domain and dynamics (jump). Note that this is a nonautonomous system because $\gamma(t)$ is a time-varying function.

Fig. 4 visualizes the flow- and jump-sets given in (5) and (6). The cones depict the vector field that results from (7) in phase space depending on the sign of γ. Directions for $\gamma \leq 0$, illustrated by the dotted quadrants of the cones, are prevented in the remainder of this paper. For $\gamma > 0$ the system is guaranteed to hit the end-effector at some point in time, but a time-varying γ may still lead to increasing velocities $x_2(t_c)$ between impacts and, thus, unstable behavior. Section III tackles stability for $\gamma > 0$ and its relation to the coefficient of restitution ρ.

As will be shown, success in open-loop nonprehensile catching corresponds to finding accelerations $\gamma(t)$ for $t \geq 0$, which provide asymptotic stability with respect to the compact set $\mathcal{A} := \{\boldsymbol{x} : x_1 = 0, x_2 = 0\}$, cf. (2), for a large set of initial relative states. A desirable, asymptotically stabilizing, 1-D solution $\gamma^*(t)$ may directly be applied to a ballistic catch using the dynamical system parameterization derived next. Conditions for $\gamma^*(t)$ to become asymptotically stabilizing are discussed in Section III.

C. Parameterization of the Ballistic Motion

Consider a reference frame denoted by orthogonal unit vectors $\hat{u}$, $\hat{v}$, and $\hat{w}$, depicted in the right part of Fig. 5. The first two unit vectors $\hat{u}$ and $\hat{v}$ are parallel to the floor. The third unit vector $\hat{w}$ is normal to the floor and, thus, aligned parallel with the direction of gravity g. Hence, during free flight, a rotation around $\hat{w}$ exists such that the velocity in $\hat{v}$-direction becomes zero. From here on we, thus, assume $\dot{v} = 0$ at all times allowing planar treatment in the $\hat{u}$-$\hat{w}$-plane of flight.
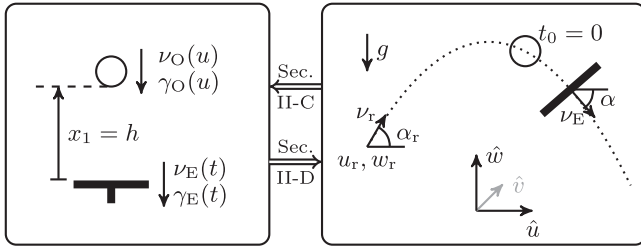
Fig. 5.   *Left:* Hybrid bouncing ball with accelerated end-effector acting as unilateral constraint. *Right:* 2-D ballistic trajectory after rotation around $\hat{w}$ such that $\hat{v}$ is normal to the flight plane. The release point is given at time $t = t_r < 0$.

Remark 1: With an appropriate rotation around $\hat{w}$, assuming $\dot{v} = 0$ is generally mild because no acceleration due to gravity occurs in $\hat{v}$-direction. In the presence of collisions, assuming $\dot{v} = 0$ is only mild for spherical objects. Due to the poor predictability of polygonal collisions, instantaneous changes of $\dot{v}$ may occur. Motion in this direction, however, may be easily countered with a box-like end-effector design and consideration of U3.

In the following, a parameterization is derived for the flight path angle α, which describes the vertical direction in the $\hat{u}$-$\hat{w}$-plane of flight. Based on the parabolic equations of ballistic flight, it is shown that the flight path angle α can be expressed as a function of the horizontal position u to describe the 1-D motion on the ballistic path. The dotted line in Fig. 5 represents such a ballistic path. This path is uniquely defined for free object flight if the object position and velocity vector is known at one point in time. Therefore, in order to define the path, the release at $t_r < 0$ with object position (u_r, w_r), object speed ν_r, and object flight path angle α_r are taken as given. Uncertainties at t_r map to U1 and are therefore included.

The object position for $t > t_r$ is

$$u(t) = u_r + \nu_r (t - t_r) \cos \alpha_r \tag{9}$$

$$w(t) = w_r + \nu_r (t - t_r) \sin \alpha_r - \frac{1}{2} g (t - t_r)^2. \tag{10}$$

For the parameterization along the ballistic trajectory, substitute the time of flight by the u-coordinate, which identifies the object state uniquely. Solving (9) for t gives

$$t(u) = \frac{u - u_r}{\nu_r \cos \alpha_r} + t_r \tag{11}$$

which is only a function of constants and the position u. Hence, velocities for a particular object trajectory can be expressed in terms of constants and u by

$$\dot{w}(u) = \nu_r \sin \alpha_r - g \frac{u - u_r}{\nu_r \cos \alpha_r} \tag{12}$$

$$\dot{u} = \nu_r \cos \alpha_r . \tag{13}$$

The flight path angle after release may be denoted by $\alpha(t)$ for $t > t_r$ or, using (11)–(13), in the parametrized form

$$\alpha(u) = \operatorname{atan}\left(\frac{\dot{w}(u)}{\dot{u}}\right) \tag{14}$$

which results in a negative α for the catching situation in Fig. 5.

Using the aforementioned parameterization in terms of u, the object acceleration in flight direction is given by

$$\gamma_O(u) = -g \sin(\alpha(u)). \tag{15}$$

The parametrized velocity of the free flying object in flight direction using (12) is given by

$$\nu_O(u) = \sqrt{\dot{u}^2 + (\dot{w}(u))^2}. \tag{16}$$

See also Fig. 5 for direction and sign conventions.

The focus in this paper, however, is on the motion an end-effector has to perform on the ballistic path in order to stabilize the nonprehensile catch. Therefore, we define a second pair of variables for end-effector acceleration γ_E and velocity ν_E. These two variables are defined on the ballistic path and are thoroughly discussed in the remainder of this paper. As $\frac{\mathrm{d}}{\mathrm{d}t} \nu_E = \gamma_E$, the acceleration γ_E is the input to the robotic catching system and $\nu_E(t_0)$ is an initial speed on the path that needs further discussion.

D. End-Effector Motion on the Ballistic Path

Here, we present the first main contribution of this paper: A dynamical system motion generator for P3 to reconstruct an end-effector trajectory $\boldsymbol{\xi} := [\, \nu_E \; u_E \; w_E \,]^\top$ from solutions $\gamma^*(t)$ of $\mathcal{H}$.

A stabilizing relative acceleration $\gamma^*(t)$ on the ballistic path of an object in the $\hat{u}$-$\hat{w}$-plane is tracked with an end-effector motion described by the nonlinear dynamical system

$$\dot{\boldsymbol{\xi}} = \boldsymbol{\phi}(t, \boldsymbol{\xi}) = \begin{bmatrix} \gamma_E(t, \xi_2) \\ \xi_1 \cos(\alpha(\xi_2)) \\ \xi_1 \sin(\alpha(\xi_2)) \end{bmatrix}, \; \boldsymbol{\xi}_0 = \boldsymbol{\xi}(t = 0) \tag{17}$$

with acceleration $\gamma_E(t, \xi_2) = \gamma_O(\xi_2) - \gamma^*(t)$ and α from (14) evaluated at $\xi_2 = u_E$. Hereby, the first state $\xi_1 = \nu_E$ is the 1-D end-effector velocity on the ballistic path, whereas the other two states determine the position of the end-effector in the plane of flight, cf., Fig. 5.

The initial end-effector state is defined

$$\boldsymbol{\xi}_0 = \begin{bmatrix} \nu_O(0) + x_2(0) \\ u(0) + (x_1(0) + r) \cos(\alpha(0)) \\ w(0) + (x_1(0) + r) \sin(\alpha(0)) \end{bmatrix} \tag{18}$$

using (9), (10), (14), and (16). The scalar r denotes the radius of the object circumcircle and therefore ensures that the object and end-effector are initially disjoint.[3] Note also that (18) is based on the assumption of sufficiently small $(x_1(0) + r)$, which allows to assume $\gamma_O(u_E) \cong \gamma_O(u)$ in the remainder of this paper. For a given initial end-effector state $\boldsymbol{\xi}_0$, the desired end-effector trajectory $\boldsymbol{\xi}(t)$, thus, results from a numeric integration of (17) with input $\gamma^*(t)$.

Section III analyzes and discusses the influence of γ on bouncing ball dynamics and, thus, on robotic catching. The choice of

---

[3]If a range of differently sized objects should be caught with the same setup, one may simply choose r from the largest possible object at the cost of increasing U1.

the relative initial state $\boldsymbol{x}(0)$ is crucial for the success of an open-loop catch and will be discussed in Section IV. As a result, Section V proposes an optimization-based motion planner for robotic catching that finds $\gamma^*(t)$ while taking dynamic limitations of the robot into account.

III. STABILIZING RELATIVE MOTIONS

In this section, we regard stability of the 1-D bouncing ball (5)–(8) in the presence of U1–U3. First, the theorem of Or *et al.* [35] on uniform Zeno asymptotic stability (UZAS)[4] is reviewed. Then, we derive a corollary on the maximum possible rebound height for the UZAS system. At the end of the Section, an academic example illustrates robustness of the presented theory to U1–U3.

A. Review of Uniform Zeno Asymptotic Stability

Consider the hybrid dynamical system $\mathcal{H}$ from (5)–(8) with set-valued acceleration

$$\gamma(t) \in [\gamma_{\min}, \gamma_{\max}], \quad \text{where } 0 < \gamma_{\min} \leq \gamma_{\max}. \quad (19)$$

Or *et al.* then proved the following theorem in [35].

Theorem 1 (Or et al. [35, Th. 1]): The origin of a bouncing ball $\mathcal{H}$ with set-valued acceleration (19), possesses uniform Zeno stability if and only if

$$\rho^2 < \frac{\gamma_{\min}}{\gamma_{\max}} \quad (20)$$

holds.

For the detailed proof refer to [35]. Here, we sketch and discuss the major steps of the proof, which allow a novel view on the robustness problem formulated in U1–U3.

The proof relies on a sophisticated Lyapunov function $V : U \to \mathbb{R}_{\geq 0}$ with $U = \{\boldsymbol{x} \in \mathbb{R}^2 : W(\boldsymbol{x}) > 0\}$ defined by

$$V(\boldsymbol{x}) = \kappa x_2 + \sqrt{W(\boldsymbol{x})}, \quad \text{where } W(\boldsymbol{x}) = \frac{1}{2p(x_2)} x_2^2 + x_1$$

with $p(x_2) = \begin{cases} \gamma_{\max}, & \text{if } x_2 \leq 0 \\ \gamma_{\min}, & \text{if } x_2 > 0 \end{cases}$

and $\kappa = \left(\frac{1}{\sqrt{2\gamma_{\max}}} - \frac{\rho}{\sqrt{2\gamma_{\min}}} \right) \frac{1}{1+\rho}. \quad (21)$

Interestingly this piecewise defined Lyapunov function is continuous and continuously differentiable on $\mathrm{dom}\, V$ even though kinetic energy is deducted instantaneously from the hybrid bouncing ball system at every collision

$$V(g(\boldsymbol{x})) = V(\boldsymbol{x}) \quad (22)$$

for all $\boldsymbol{x} \in D$. Furthermore, by verifying that

$$\langle \nabla V(\boldsymbol{x}), \boldsymbol{f} \rangle \leq -\kappa \gamma_{\min} \quad (23)$$

holds for all $\boldsymbol{x} \in C \backslash \{0\}$, one concludes that $V(\boldsymbol{x})$ is a strictly decreasing Lyapunov function. Therefore the origin is UZAS.

[4]Zeno behavior describes the occurrence of infinitely many impacts in a finite amount of time. Formal definition, e.g., in [35, Def. 1].
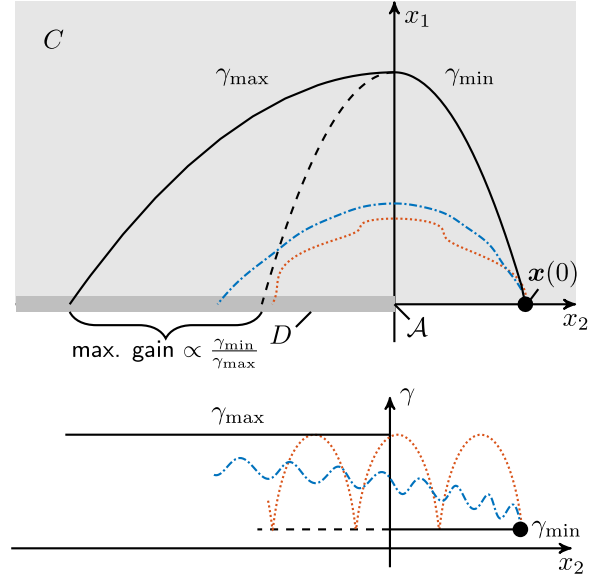

Fig. 6. Flow and jump sets of the hybrid bouncing ball $\mathcal{H}$ over a single period starting at $\boldsymbol{x}(0)$. The acceleration γ satisfies (19) and (20). Any fast or slowly varying acceleration within the bounded set leads to a lower rebound height than a single switch from the lower to the upper bound at the maximum height ($\gamma = -p(x_2)$), which is the "most unstable solution" [35].

For the bouncing ball follows from (19) robustness with respect to uncertain relative acceleration (U2) as visualized with single flow periods in Fig. 6. From (20) follows robustness with respect to uncertain restitution behavior (see U3). Furthermore, it becomes possible to establish continuous contact with a single open-loop acceleration $\gamma(t)$ for a range of initial states $\boldsymbol{x}(0) \in C \cup D$, which relates to U1. Hereby, $\gamma(t)$ might even be chosen constant. As a result, given a sufficiently small U1 provided by the repeatable robot throw, the approach in this paper does not require replanning of the catching motion, nor does it require real-time measurements of the object state.

B. Bounded Rebound Height

Besides the stability of system $\mathcal{H}$, we are also interested in a bound on the rebound height after an arbitrary point in time t' subject to (19) and (20). The following corollary offers an easily applicable answer. Thereby, the abbreviations for the relative height $x_1(t') =: h'$ and relative velocity $x_2(t') =: \nu'$ are used.

Corollary 1: If the acceleration $\gamma(t)$ of the hybrid bouncing ball system $\mathcal{H}$ satisfies (19) and (20) for all $t > t'$, then the maximum possible rebound height for all $t > t'$ is limited by

$$\bar{x}_1(h', \nu') = \begin{cases} h' + \dfrac{(\nu')^2}{2\gamma_{\min}} & \text{for } \nu' \geq 0 \\[2ex] \max\left[h', \dfrac{\rho^2\left((\nu')^2 + 2\gamma_{\max}h'\right)}{2\gamma_{\min}} \right] & \text{for } \nu' < 0 \end{cases} \quad (24)$$

based on the relative state $\boldsymbol{x}(t') =: [h' \; \nu']^\top$.

Proof: Due to (19), the ball reaches the highest point at zero relative velocity ($x_2 = 0$) in every rebounding cycle. Furthermore, due to the UZAS property, in every consecutive cycle

the highest point $x_1(x_2 = 0)$ is smaller than in the previous one. Hence, in order to compute $\bar{x}_1$, it is sufficient to calculate the first $x_1(x_2 = 0)$ after t' in the presence of the worst case acceleration scenario given by $p(x_2)$ in (21).

The first case in (24) represents the rising phase, i.e., $\nu' \geq 0$. Here, we simply take the current height h' in addition to the height that could be gained by transforming the current kinetic energy into potential energy under the smallest possible acceleration.

In the falling case $\nu' < 0$, a collision occurs before the next peak height is reached. Denoting the first postimpact velocity after t' as ν^+, we already know from the previous step with $h' = 0$ that $\bar{x}_1 = \frac{(\nu^+)^2}{2\gamma_{\min}}$. With the restitution law $\nu^+ = -\rho\nu^-$ the relation to the preimpact state becomes

$$\bar{x}_1 = \frac{(-\rho\nu^-)^2}{2\gamma_{\min}}. \tag{25}$$

Finally, the maximum possible velocity of ν^- is what we get from the kinetic energy of ν' in addition to the velocity gained by transforming h' into kinetic energy under the largest possible acceleration

$$\nu^- = -\sqrt{(\nu')^2 + 2\gamma_{\max}h'}. \tag{26}$$

Inserting (26) in (25) results in the second line of (24), considering that $\bar{x}_1$ must never be smaller than the current height h'. ∎

For acceleration ratios (20) close to one, the presented theorem and corollary are not restrictive because nearly the full range of the coefficient of restitution ρ is allowed. Vice versa, the restrictions on ρ become tight if a large range of accelerations γ must be covered.

In nonprehensile robotic catching, we will later see that convergence speed improves as $\gamma_{\min}$ increases, which can also be concluded from (23). Large acceleration, however, may only be provided in P3 (following) because P4 (deceleration) is typically governed by comparably little acceleration. Under typical conditions the Zeno time may lie in P4, illustrated with Example 1 at the end of this section. Therefore we have to deal with a restrictively large range of accelerations.

C. Illustrative Example and Discussion

During P3 the robot tracks the ballistic flight path and is capable to produce a large relative acceleration. The tracking duration of P3 is limited by the kinematic and dynamic constraints of the robot. If tracking is not possible anymore, P4 starts and provides only low relative acceleration. Here, we present a realistic example to discuss UZAS from Theorem 1 and the novel Corollary 1 focusing on uncertainty U2 in P3 and P4.

Example 1: Consider a relative initial state $\boldsymbol{x}(0) = \begin{bmatrix} 0 & 0.9 \end{bmatrix}^\top$ at start of P3, which means the hybrid bouncing ball $\mathcal{H}$ is initially in contact and has positive velocity. The restitution is chosen $\rho = 0.35$. In P3, the robot moves according to (17) with the goal to apply $\gamma^* = 25 \text{ ms}^{-2}$. In P4, the goal is to maintain previously established contact with $\gamma > 4 \text{ ms}^{-2}$. Two acceleration patterns are simulated to represent U2 in the presence of these goals. Both are depicted in the lower plot of Fig. 7. The solid line
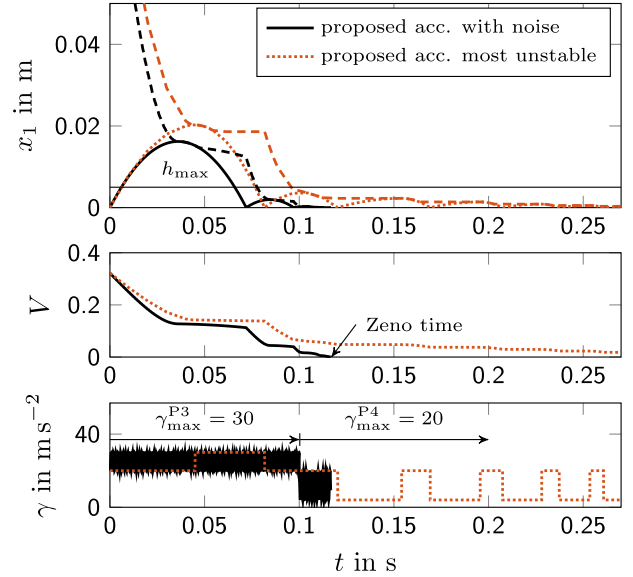

Fig. 7. Height of a bouncing ball over time with initial state $\boldsymbol{x}(0) = \begin{bmatrix} 0 & 0.9 \end{bmatrix}^\top$ and restitution $\rho = 0.35$. The dashed lines in the upper plot indicate the respective upper bound $\bar{x}_1$ from (24), which is decreasing. The Lyapunov function (middle) based on (21) is continuous and decreasing to zero in finite (Zeno) time. Dynamics after the Zeno time are not considered. The upper acceleration bound $\gamma_{\max}$ drops at $t_f = 0.1$ s, which accounts for limited robot tracking capabilities.

shows a simulation of noisy acceleration by means of a high-frequent sine function between 20 ms^{-2} and 30 ms^{-2} in P3 and between 4 ms^{-2} and 20 ms^{-2} in P4. The dotted line depicts a simulation of the "most unstable acceleration" [35] that is $\gamma = -p(x_2)$ using the previously mentioned bounds.

The first two plots of Fig. 7 show the simulation result for height and Lyapunov function value (21) over time for a sequence of impacts. The fast variations of γ, which intend to simulate noise, are not visible in the two upper plots, which is due to the low pass property of the double integrating flow. Moreover, the Lyapunov function value decreases faster during $t < 0.1$ s, which is in line with (23) and, thus, we conclude that large $\gamma_{\min}$ is desirable.

In addition, the first plot also displays the evaluation of Corollary 1 with dashed lines. For this evaluation, uncertainty U2 and the drop in relative acceleration at $t = 0.1$ s is taken into account by $\gamma_{\max}^{\text{P3}} = 30 \text{ ms}^{-2}$ and $\gamma_{\min}^{\text{P3}} = 4 \text{ ms}^{-2}$, which reduces to $\gamma_{\max}^{\text{P4}} = 20 \text{ ms}^{-2}$ and $\gamma_{\min}^{\text{P4}} = 4 \text{ ms}^{-2}$ for $t > 0.1$ s. At the example of a maximum rebound height $h_{\max} = 5$ mm, indicated by the horizontal line in the first plot of Fig. 7, one can see that (24) already holds from $t = 0.1$ s. The simulated Zeno time here is at $t = 0.34$ s in the most unstable case. Limiting the analysis to only those solutions that have Zeno times that lie in P3 might, thus, be overly restrictive. Hence, Section IV will introduce a box-like end-effector and analyze the maximal Zeno time in a formal way.

IV. TOWARD PREDICTABLE SUCCESS

So far, solving the general catching problem (2) in the presence of U1–U3 robustly has become possible using (17) and

(20). Nonetheless, Example 1 illustrates that the lack of relative acceleration in P4 leads to a large range $\gamma(t) \in [\gamma_{\min}, \gamma_{\max}]$ if (20) has to consider potential acceleration changes in both P3 and P4. Furthermore, the end-effector has been considered planar. In practice, relative motions perpendicular to the distance measure h inevitably occur. Therefore, we here discuss a restriction of (2) to increase practical applicability and we discuss to what extend a box shaped end-effector allows negligence of motions perpendicular to h.

A. Success Prediction Based on the Maximal Zeno Time

The UZAS condition (20) formulates if the general catching goal (2) can be achieved as $t \to \infty$ and, thus, if a finite Zeno time Z exists. Consequently, the notion of a maximal Zeno time [35] becomes also applicable.

Theorem 2 (Or et al. [35, Th. 2]): If condition (20) is satisfied, all solutions are Zeno and their maximal Zeno time is given by

$$Z_{\max}(h', \nu') = \begin{cases} \dfrac{\nu' + \sigma U_{0,\min}}{\gamma_{\min}} & \text{for } \nu' \geq \nu_c \\ \dfrac{\nu' + U_{0,\max}(1 + \beta\delta)}{\gamma_{\max}} & \text{for } \nu' < \nu_c \end{cases} \quad (27)$$

where

$$U_{0,\max} = \sqrt{(\nu')^2 + 2\gamma_{\max}h'}$$

$$U_{0,\min} = \sqrt{(\nu')^2 + 2\gamma_{\min}h'}$$

$$\nu_c = -\sqrt{\frac{2\gamma_{\min}h'}{\sigma^2 - 1}}, \quad \delta = \frac{\gamma_{\max}}{\gamma_{\min}}$$

$$\beta = 2\rho\frac{1 + \rho}{1 - \rho^2\delta}, \quad \sigma = \sqrt{1 + 2\beta + \delta\beta^2}. \quad (28)$$

Proof: See proof in [35, Th. 2]. ∎

In practice, the general formulation with $t \to \infty$ evaluated at $t = 0$ s requires to consider acceleration changes in both phases P3 and P4. Large values $Z_{\max}$ and small valid ranges for ρ are the result. Therefore, we here propose the limitation of the time horizon to the tracking phase P3 with controllable relative acceleration. The general catching goal (2), thus, reformulates to

$$h(t \to t_f) = 0 \quad \text{and} \quad \nu(t \to t_f) = 0. \quad (29)$$

Hence, successful catching becomes predictable for initial relative states that fulfill $Z_{\max}(\boldsymbol{x}(0)) < t_f$, also subject to U1–U3.

Example 1 (revisited): Consider the acceleration range of P3 as described in Example 1 and restitution $\rho = 0.35$. Fig. 8 then visualizes the maximal possible Zeno time (27) at the start of P3 ($t_0 = 0$) depending on the initial relative state $\boldsymbol{x}(0)$. The solid contour indicates $Z_{\max} = 0.1$ s, which allows to conclude that all initial relative states enclosed by this contour and the horizontal axis fulfill (29), and, thus, lead to continuous contact already in P3. The dash-dotted contour indicates the effect of U3, which illustrates that (27) is monotonically decreasing (admissible U1 fulfilling $Z_{\max} < t_f$ increases) as ρ decreases.

Hence, the proposed approach applies for all potential restitutions below ρ and, thus, provides robustness for a range of ma-
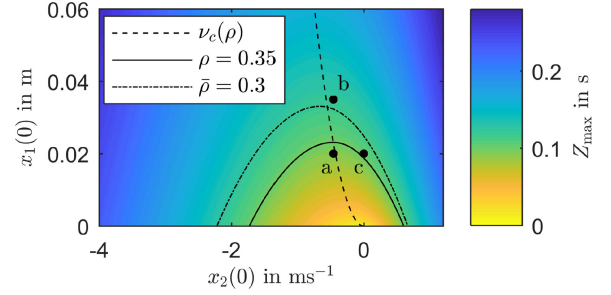

Fig. 8. Contours indicating the maximal Zeno time (27) for Example 1 acceleration bounds in P3 $\left(\gamma(t) \in [20, 30] \text{ ms}^{-2}\right)$ subject to the initial relative state $\boldsymbol{x}' = \boldsymbol{x}(0)$ and $\rho = 0.35$. All initial states below the solid contour fulfill $Z_{\max} < t_f = 0.1$ s. The dash-dotted contour indicates the trend of the $Z_{\max} < t_f$ contour as ρ decreases.

terials (U3) without need for replanning. Even more important is the resulting potential to overcome the problem of the difficult and imprecise estimation of an object dependent restitution behavior.

From the revisited example, it becomes clear that in the presence of U1–U3 a robust initial relative state $\boldsymbol{x}^{\text{rob}}(0)$ must lie in the center of the area enclosed by the solid contour in Fig. 8. The best choice for a nominal initial state, however, depends on the expected magnitude in each dimension of U1. Nonetheless, the following corollary gives an orientation for potentially good nominal initial relative velocities. In view of Fig. 8, the following corollary returns the velocity $x_2(0)$ for which the solid parabolic contour reaches the maximal $x_1(0)$-value.

Corollary 2: Assume condition (20) is satisfied, then the nominal initial relative velocity

$$x_2^{\text{rob}}(0) = -\frac{\gamma_{\min}Z_{\max}}{2\beta + \delta\beta^2} \quad (30)$$

maximizes the range of $x_1(0)$ for which (29) holds, where $Z_{\max} = t_f - t_0$ is the duration of P3 and β is calculated based on the maximum expected restitution in h-direction.

Proof: First, rearrange the first case in (27) to become a function of $Z_{\max}$ and ν given by

$$h = \frac{(1 - \sigma^2)\nu^2 - 2\gamma_{\min}Z_{\max}\nu + (\gamma_{\min}Z_{\max})^2}{2\sigma^2\gamma_{\min}}. \quad (31)$$

Then, take the derivative

$$\frac{\mathrm{d}h}{\mathrm{d}\nu} = \frac{(1 - \sigma^2)\nu - \gamma_{\min}Z_{\max}}{\sigma^2\gamma_{\min}} \quad (32)$$

where setting (32) equal to zero results in

$$\nu = \frac{\gamma_{\min}Z_{\max}}{1 - \sigma^2} = -\frac{\gamma_{\min}Z_{\max}}{2\beta + \delta\beta^2}. \quad (33)$$

Considering that $\sigma^2 > 1$, a second derivative $\frac{\mathrm{d}^2h}{\mathrm{d}\nu^2}$ will always be negative and thus (33) is a maximum.[5] Repeating steps (31)–(33) for the second case in (27) returns the same result. ∎

---

[5] Note here that (33) is directly related to ν_c in (28), e.g., by inserting the first case of (27) into (33) and resolving for ν.
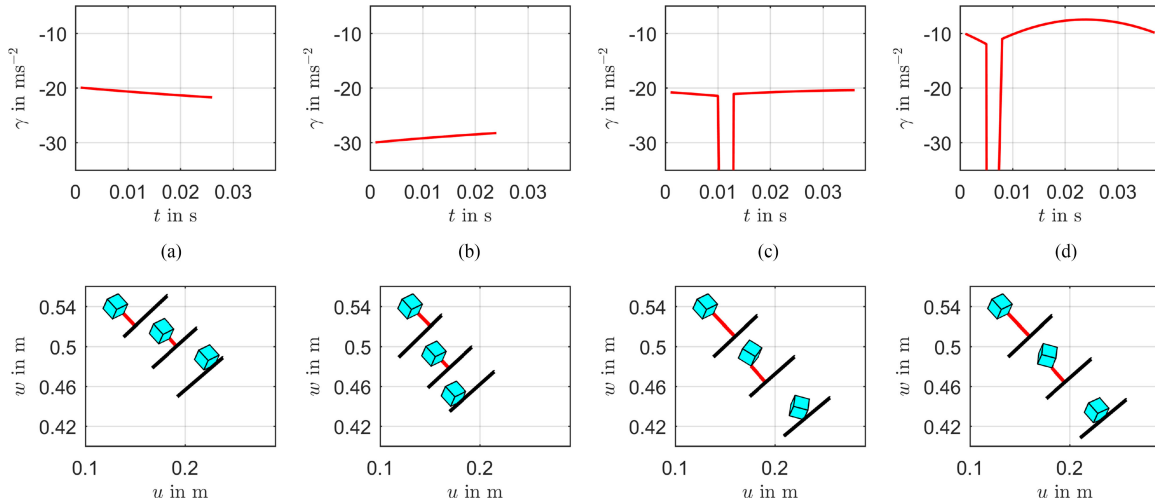
Fig. 9. Simulation results of Example 2 to evaluate the influence on the relative acceleration in h-direction of motions perpendicular to h (a) and (b) and of object rotation (c) and (d). In (a) and (b), the motion perpendicular to h has a magnitude of 1.4 ms^{-1} for which it stays within the previously assumed acceleration bounds. In (c), the rotation of 20 rad s^{-1} about one object axis does not violate the acceleration bounds, except for the moment when the nearest edge of the object switches. In (d), the rotation of 40 rad s^{-1} about one object axis leads to permanent violation of the acceleration bounds.

As a result, we recommend to first target a relative velocity according to Corollary 2 for the motion planning of future catching robots as the knowledge of object states is inevitably imprecise (U1). For example due to object state estimation errors of vision systems or blind throwing robots, neglected aerodynamic drag or unknown object shape. Hence, a negative offset for $x_2(0)$, besides providing the necessary negative relative acceleration ($\gamma > 0$), is suggested as primary measure to increase success in robotic catching. If reliable success is achieved, one may then further reduce impact velocities with velocity matching $x_2(0) \to 0$, as considered in most previous dynamic catching approaches of lower success rate.

B. Previously Neglected Motions in View of Arbitrary Shapes

In this paper, the velocity components of the object perpendicular to the distance measure h are neglected during parameterization and stability analysis. But, such parallel motions slowly start to occur for $t > 0$ and become nonnegligible in magnitude when the end-effector has to move away from the ballistic path with start of P4. In case of nonspherical objects, already the first collision in P3 may induce significant motions perpendicular to h. We, here consider the following three major issues related to motions perpendicular to h.

1) Unpredictable Velocity Transformation: Rotation or velocities perpendicular to h may be transformed into velocity in h-direction at collisions, whereas the outcome of such collisions with objects of arbitrary shape is hardly predictable. Even coefficients of restitution $\rho > 1$ in h-direction are likely to occur. On the other hand, frictional losses tend to be higher for polygonal objects compared to spherical ones. Therefore, calculations from the previous section cannot predict success or failure for arbitrarily shaped objects in a quantitative way. Nonetheless, Theorem 2 and Corollary 2 allow to analyze the qualitative effect of many variables. In order to regain explicitness lost through impacts, the object state after collisions, or at

least h and ν, must be measurable. Taking such measurements is a challenge itself, especially for small rebounds and, thus, lie beyond the scope of this paper.

2) Effect on Acceleration Uncertainty (U2): Rotation or velocities perpendicular to h are the major source of U2, including errors and unmodeled changing tilt angles of the end effector. The presented theorems and corollaries all rely only on the boundedness of the relative acceleration $\gamma(t)$, which already includes robustness against U2. They do explicitly not require knowledge of a particular acceleration pattern. Therefore, the goal here is to exemplary study the influence of previously neglected effects on the range of occurring relative accelerations.

Example 2: Consider a cube-object starting above the end-effector as depicted in Fig. 9. Four scenarios are simulated whereas the end-effector motion is always planned for constant $\gamma^*(t) = 25$ ms^{-2}. Motions described in this second issue, thus, cause all the deviation of relative acceleration in the upper plots of Fig. 9. The initial absolute part velocity in h-direction is chosen $\nu_O = 3.5$ ms^{-1} and the initial relative velocity is chosen $\nu(0) = -0.3$ ms^{-1}. In the first two scenarios, the relative velocity perpendicular to h has, thus, a comparably large magnitude being chosen 1.4 ms^{-1}. As can be seen in the acceleration plots, the deviation from γ^* in this simulation is at most 5 ms^{-2}. Hence, the conservative choice of acceleration bounds used in Example 1 covers a notably large range of unmodeled velocities perpendicular to h. The other two scenarios (c-d) in Fig. 9 illustrate the effect of rotation on the relative acceleration $\gamma(t)$. In view of (1) and its derivatives, the closest vertex can switch, resulting in a velocity jump and, thus, very large relative acceleration instants. Therefore, nonspherical parts temporarily violate (20) here. Very fast rotations as shown in scenario (d) as well as very fast velocities perpendicular to h can even lead to permanent violations.

As Example 2 illustrates, the notion of set-valued acceleration introduced with (19) compensates a considerable range of
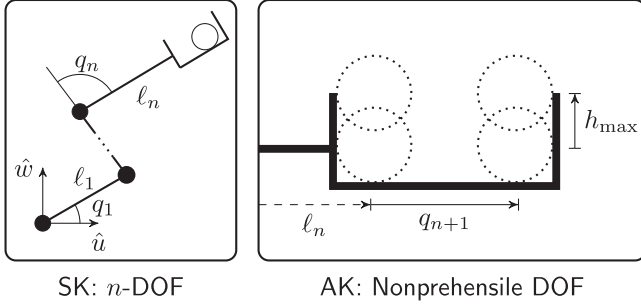
Fig. 10. *Left:* Kinematic model for n actuated rotational degrees of freedom. The $\hat{u}$-$\hat{w}$-frame coincides with the robot base. *Right:* Unactuated, box-like end-effector with height $h_{\max}$ and prismatic joint as "virtually" actuated DOF q_{n+1}.

Fig. 11. Contours indicating the maximal possible rebound height (24) for Example 1 acceleration bounds $\left(\gamma(t) \in [20, 30] \text{ ms}^{-2}\right)$ at the end of P3 ($t' = t_f$) and subject to $\rho = 0.35$. All initial states below the solid contour fulfill $\bar{x}_1(h_f, \nu_f) = 0$ mm (Zeno solutions). The dash-dotted contour depicts the $\bar{x}_1(h_f, \nu_f) < 5$ mm contour.

rotational and translational velocities neglected in Sections II and III.

3) Limited End-Effector Domain: The object may leave the limited domain of a planar end-effector.

So far, the end-effector has been assumed planar like a plate. However, even if (29) holds and no form or force closure is used, the object may start to roll or slide on the end-effector after entering P4. Therefore, we propose the box-like end-effector design in Fig. 10 to prevent objects from falling off. Moreover, such motions parallel to $\mathcal{S}_E$ have an additive or subtractive effect (depending on the direction) on the relative acceleration between the object and end-effector, similar to what has been analyzed with Example 2. Contact with the box walls may even induce additional velocity. In order to prevent the object from losing contact with $\mathcal{S}_E$, motion planning in P4 must pursue sufficiently large negative relative acceleration.

In case of spherical objects and in view of Corollary 1, a box-like end-effector may even enable successful catching if

$$\bar{x}_1(h', \nu') < h_{\max} \quad \text{at} \quad t' = t_f \tag{34}$$

holds, whereas $h_{\max}$ denotes the box height reduced by the object radius, cf., Fig. 10. Again, we revisit Example 1 to quantify the effect of the box height with the help of Corollary 1.

Example 1 (revisited): Consider the acceleration range of P3 as described in Example 1, restitution $\rho = 0.35$ and the same range of potential initial relative states as in Fig. 8. A simulation now calculates how the relative object state x evolves until $t_f = 100$ ms based on the "most unstable" acceleration pattern illustrated in Fig. 7. At time $t = t_f$, Corollary 1 is evaluated for all $x(t_f) = [\, h_f \; \nu_f \,]^\top$ using $\gamma_{\max}^{P4} = 20 \text{ ms}^{-2}$ and $\gamma_{\min}^{P4} = 4 \text{ ms}^{-2}$. Fig. 11 illustrates the results.

Similar to the discussion in Section IV-A, negative relative velocities turn out advantageous as rebounds remain comparably small with respect to distance uncertainties.

V. FEASIBLE MOTIONS

In this section, we present an optimization-based motion planning approach to realize the stability concept from Section III in the ballistic catching scenario. In order to maintain stability claims, kinematic and dynamic feasibility of end-effector motions is always guaranteed. Therefore, the section begins with a
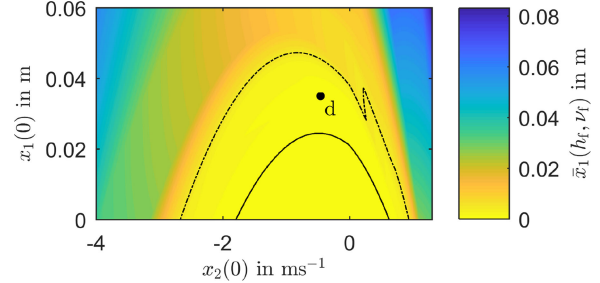
standard formulation of the dynamic model. It follows an augmentation of the related standard kinematic (SK) description with an additional, "virtual" degree of freedom, enabled by the nonprehensile approach.

A. Kinematic and Dynamic Model

Here, we formulate the n-DOF dynamics of a serial manipulator and an augmentation to $(n + 1)$-DOF kinematics. The augmentation results from the nonprehensile approach because the end-effector provides a range of possible contact points.

1) Standard Kinematics (SK) and Dynamics: Consider a robot with n actuated rotational degrees of freedom $\bar{q} \in \mathbb{R}^n$ as shown in Fig. 10 on the left. The dynamic equations for this serial robotic structure have the well known form

$$M(\bar{q})\ddot{\bar{q}} + C(\bar{q}, \dot{\bar{q}})\dot{\bar{q}} + G(\bar{q}) = \tau \tag{35}$$

with the mass matrix $M \in \mathbb{R}^{n \times n}$, the Coriolis matrix $C \in \mathbb{R}^{n \times n}$, the gravitational vector $G \in \mathbb{R}^n$, and the input torque $\tau \in \mathbb{R}^n$. This paper will demonstrate that $n = 2$ is sufficient for the dynamically challenging task of robotic catching using the following augmentation.

2) Augmented Kinematics (AK): The augmentation is motivated by preliminary investigations for the 2-DOF SK in our experimental setup. With 2-DOF no redundancy, except for the choice between over- and underarm configuration, exists given the ballistic path and a desired end-effector acceleration on this path. The motion of a ball thrown from an exemplary distance of 1.77 m cannot be tracked. In order to find a joint trajectory $\bar{q}(t)$ that is nonetheless kinematically and dynamically feasible, we exploit the nonprehensile DOF. surface of the end-effector. So, the contact point is an extra degree of freedom, though not actuated. For an extensive evaluation of kinematic augmentation in nonprehensile scenarios, the reader may refer to [36].

In the planar catching scenario, it is sufficient if any point of the end-effector surface tracks the desired trajectory. In other words, the ball can land anywhere on the surface of the end-effector. So, the contact point is an extra degree of freedom, though not actuated. We account for this by augmenting the kinematic model with an additional, virtually actuated prismatic DOF $q = \left[\, \bar{q}^\top \; q_{n+1} \,\right]^\top$, as visualized in Fig. 10.

The newly introduced redundancy is resolved using a normalized cubic Hermite spline

$$q_{n+1}(t, t_f, \boldsymbol{p}) = \frac{1}{t_f^3} \left(2p_1 - 2p_2 + t_f p_3 + t_f p_4\right) t^3$$

$$- \frac{1}{t_f^2} \left(3p_1 - 3p_2 + 2t_f p_3 + t_f p_4\right) t^2 + p_3 t + p_1 \quad (36)$$

on the interval $t \in [0, t_f]$ with 0 and t_f being the start and end of P3 (see Fig. 2), respectively. The vector $\boldsymbol{p} \in \mathbb{R}^4$ collects the polynomial coefficients. With the Hermite spline (36), the last joint is later constrained intuitively as the coefficients $\boldsymbol{p} :=$ $\begin{bmatrix} q_{n+1}(0) & q_{n+1}(t_f) & \dot{q}_{n+1}(0) & \dot{q}_{n+1}(t_f) \end{bmatrix}^\top$ are the displacement and the velocity of q_{n+1} at start and end of P3.

Given a particular parameterization $\boldsymbol{p}$, a standard inverse kinematic problem for the first n joints of $\boldsymbol{q} \in \mathbb{R}^{n+1}$ with

$$\boldsymbol{q}(t) = \boldsymbol{\zeta}(t, u_E(t), w_E(t), \boldsymbol{p}, t_f) \quad (37)$$

remains. In case of $n = 2$ the overarm configuration is chosen. The first time derivatives of u_E and w_E are known from the solution of (17). The second time derivative is calculated by means of a numeric forward differentiation. Hence, the first and second order differential inverse kinematics are uniquely defined by

$$\dot{\boldsymbol{q}}(t) = \boldsymbol{J}^{-1} \begin{bmatrix} \dot{u}_E & \dot{w}_E \end{bmatrix}^\top \quad (38)$$

$$\ddot{\boldsymbol{q}}(t) = \boldsymbol{J}^{-1} \left(\begin{bmatrix} \ddot{u}_E & \ddot{w}_E \end{bmatrix}^\top - \dot{\boldsymbol{J}} \dot{\boldsymbol{q}} \right) \quad (39)$$

with the Jacobian $\boldsymbol{J}$ and its elementwise analytic time derivative $\dot{\boldsymbol{J}}(\boldsymbol{q}, \dot{\boldsymbol{q}}) = \frac{\mathrm{d}}{\mathrm{d}t} \boldsymbol{J}(\boldsymbol{q})$. Note that we do not need to consider singularities here, because such solutions are rejected by the optimization performed next.

B. Kinematic and Dynamic Constraints

In order to maintain kinematic and dynamic feasibility with the optimization-based motion planning approach, torque,[6] power, and angular velocity limits are defined in

$$\boldsymbol{0} \geq \boldsymbol{h}(\boldsymbol{q}, \dot{\boldsymbol{q}}, \boldsymbol{\tau}) = \begin{bmatrix} |\boldsymbol{\tau}(t)| - \boldsymbol{\tau}_{\max} \\ \boldsymbol{\tau}(t) \dot{\boldsymbol{q}}(t) - P_{\max} \\ |\dot{\boldsymbol{q}}(t)| - \dot{\boldsymbol{q}}_{\max} \end{bmatrix} \in \mathbb{R}^{3n}. \quad (40)$$

The constraints in $\boldsymbol{h}$ apply in all motion planning phases. Using $q_{\mathrm{sum}} = \sum_{i=1}^{n} q_i(t)$, the vector

$$\boldsymbol{0} \geq \boldsymbol{h}^{(3)}(\boldsymbol{q}, \dot{\boldsymbol{q}}, \boldsymbol{\tau}) = \begin{bmatrix} q_{\mathrm{sum}} - q_{\max} \\ -q_{\mathrm{sum}} + q_{\min} \\ -q_{n+1}(t) \\ q_{n+1}(t) - q_{n+1, \max} \\ \dot{\boldsymbol{q}}(t_f) - \dot{\boldsymbol{q}}_{\min} \end{bmatrix} \in \mathbb{R}^{4+n} \quad (41)$$

[6]Due to the use of gears, bushed dc motors and a power consideration on mechanical level, deceleration at high velocities is supported by large frictional effects. The negative torque limit is therefore more restrictive in all relevant situations than a negative power limit.

TABLE I
PARAMETER AND CONSTRAINT VALUES FOR 2-DOF

Symbol	Value	Quantity
ℓ_1	0.315 m	Length of 1st link
ℓ_2	0.320 m	Length of 2nd link
ρ	0.35	Coefficient of restitution
r	0.015 m	Ball radius
g	9.81 m s^{-2}	Gravitational constant
$\Delta\gamma$	10 m s^{-2}	Acceleration range
α_{r}	37°	Release angle
t_{r}	−0.534 s	Release time
u_{r}	−1.770 m	Hor. release position
w_{r}	0.525 m	Vert. release position
ν_{r}	4.50 m s^{-2}	Release velocity
$x_1(0)$	0.02 m	Initial relative height
$x_2(0)$	−0.68 m s^{-1}	Initial relative velocity
$\tau_{1,\max}$	54 Nm	Peak torque limit joint 1
$\tau_{2,\max}$	38 Nm	Peak torque limit joint 2
$\ddot{q}_{\min}$	0.4 rad s^{-1}	Min. rot. speed at transition
$\ddot{q}_{\max}$	6.5 rad s^{-1}	Max. rot. speed
P	120 W	Max. motor power
$q_{\min}$	0°	Box open in flight dir.
$q_{\max}$	90°	Box open in flight dir.
$q_{3,\max}$	0.015 m	Tangential box size
$h_{\max}$	0.005 m	Normal box size (height)
N	50	Constraint evaluations

collects kinematic constraints particularly for the most important P3, indicated by the superscript $^{(3)}$. The first pair in (41) constrains the sum of joint angles to ensure that the end-effector box is opened in the direction of the approaching ball, e.g., compare the SK in Fig. 10 and the right-hand robot in Fig. 18. In case of more than two actuated DOF, the first pair in (41) may be replaced by an equality constraint that restricts the angle between the end-effector's normal vector (cf., [9]) and $\hat{w}$ to $\alpha(u_E)$. As a result, relative velocities perpendicular to h, and therefore U1 and U2, would reduce. The second pair of constraints is the length of the virtual prismatic joint q_{n+1}. Note that its derivatives $\dot{q}_{n+1}$ and $\ddot{q}_{n+1}$ are not constrained in $\boldsymbol{h}^{(3)}$, which can then be exploited by an optimization program. The constraint parameters of the robots used in this paper are presented in Table I. The dynamic limits therein are chosen below the hardware specification to leave an action margin for the low-level joint controller after the optimization.

C. Motion Planning for P3

Most critical for nonprehensile catching is P3 (cf., Fig. 2), in which the robot end-effector follows the ballistic flight path of the ball. So far, the theorems in Section III defined, which range of the relative acceleration $\gamma(t)$ stabilizes a bouncing ball on this ballistic path. The dynamical system motion generator (17) with initial state (18) allows to reconstruct the 3-D end-effector motion. A beneficial choice of $\boldsymbol{x}(0)$ was discussed in Section IV.

Still undefined at this point are the redundancy parameters $\boldsymbol{p}$, the final time (duration) of P3 t_f, and the shape of $\gamma(t)$. These remaining design parameters must now be chosen while being implicitly constrained by (40) and (41).

Our motion planning approach is the formulation of a constrained dynamic optimization problem

$$\underset{\boldsymbol{p}, t_f, \gamma(t)}{\mathrm{minimize}} \quad -\kappa \gamma_{\min} t_f$$

$$\mathrm{s.t.} \quad (35) \text{ using } (17)\text{--}(18) \text{ and } (36)\text{--}(39)$$

$$\boldsymbol{h}(\boldsymbol{q}, \dot{\boldsymbol{q}}, \boldsymbol{\tau}) \leq \boldsymbol{0}, \ \boldsymbol{h}^{(3)}(\boldsymbol{q}, \dot{\boldsymbol{q}}, \boldsymbol{\tau}) \leq \boldsymbol{0} \quad (42)$$
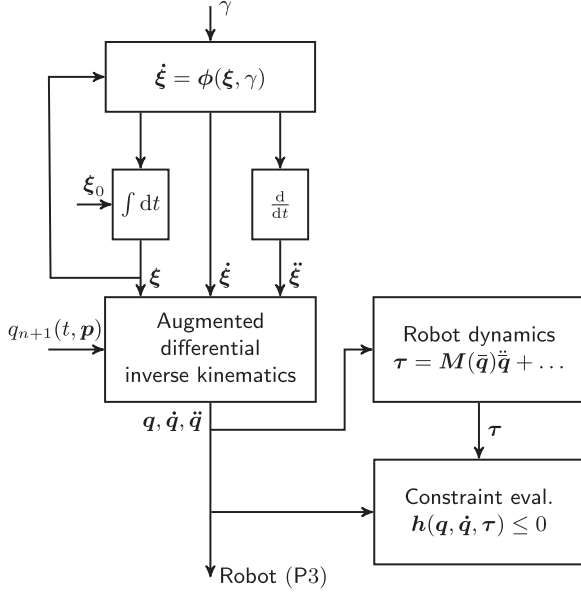
Fig. 12. Block diagram visualizing the generation of the workspace motion by (17) based on γ and $\boldsymbol{\xi}_0$. Using the augmented differential inverse kinematics together with $\boldsymbol{p}$, the motion translates into joint space and the constraints for the dynamic optimization problem (42) are obtained.

visualized in Fig. 12. The chosen cost function partially originates in (23), which quantifies the convergence speed of the Zeno behavior that inevitably occurs during any nonideal contact transition. We then propose to multiply the quantified convergence speed with t_f to maximize robustness. The most important property of this cost function is its independence from the initial relative state $\boldsymbol{x}(0)$, which accounts for the use in an uncertain environment. Nonetheless, it should be noted that a desired $\boldsymbol{x}(0)$ needs to be chosen for initializing the integration of (17) with (18) during constraint handling.

In order to solve the problem as a static optimization problem with one of the many available solvers[7] the acceleration $\gamma(t)$ needs to be parametrized and constraints evaluated at discrete time steps. Here, we simply choose γ constant and consider an acceleration uncertainty $\gamma_{\min} = \gamma - \Delta\gamma$ and $\gamma_{\max} = \gamma + \Delta\gamma$. The dynamic constraints are evaluated at N equally distributed discrete points in time $t_k = \frac{t_f k}{N-1}$, $k = 0, 1, \dots N - 1$. The vector of constraints, thus, enlarges to $\boldsymbol{h} \in \mathbb{R}^{(3n+4)N+n}$.

Many other choices for $\gamma(t)$ and the other optimization variables are possible and depend on the requirements of the application. For example, the release state at time t_r on the throwing side could be added in order to adapt the ballistic trajectory to the dynamic capabilities of the catching robot or the dynamics could be parametrized to optimize the catching robot for this particular task at the design stage.

Example 3: Consider the release point, angle and velocity given as in our experiment $(n = 2)$ with $u_r = u(t_r) = -1.77$ m, $w_r = w(t_r) = 0.52$ m, $\alpha_r = 37°$, and $\nu_r = 4.50$ ms^{-1}. The optimization variables are constrained by the values in Table II. The inequality constraints $\boldsymbol{h}$ from (40) are discretized over time with $N = 50$. Solving (42)

[7]We use Sequential Quadratic Programming (SQP) in MATLAB.

TABLE II
BOUNDS ON THE OPTIMIZATION VARIABLES

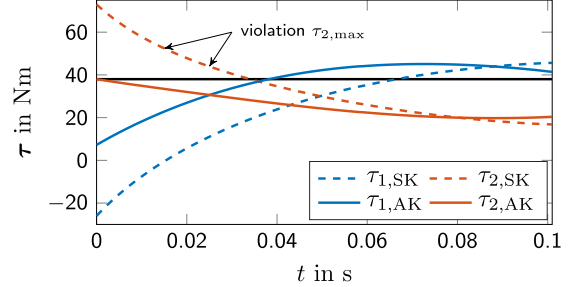| Symbol	p_1	p_2	p_3	p_4	t_f	γ
Unit	m	m	ms^{-1}	ms^{-1}	s	ms^{-2}
Upper	0.015	0.015	2	2	0.25	45
Lower	0	0	−2	−2	0.05	15

Fig. 13. Required torque of the two actuated joints to perform the P3 motion in Example 3. While the motion governed by the AK stays within the limits of $\tau_{1,\max} = 54$ N·m and $\tau_{2,\max} = 38$ N·m, a following motion with the standard 2-DOF kinematics would be dynamically infeasible.
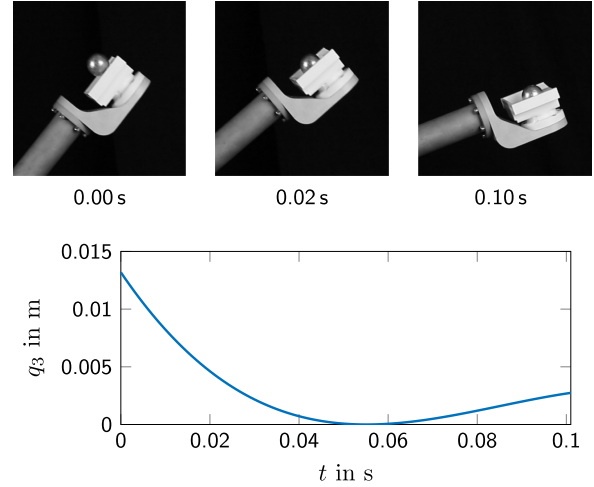

Fig. 14. Exploitation of nonprehensile augmented DOF q_3 in Example 3. The frames visualize how the end-effector is used to track the ball's flight path in P3.

then results in $\kappa\gamma_{\min}t_f = 0.12$, a constant relative acceleration $\gamma^*(t) = 39.5$ ms^{-2} and P3 duration $t_f = 0.101$ s. For the augmented DOF the optimization returns $\boldsymbol{p} = \begin{bmatrix} 0.013 \text{ m} & 0.003 \text{ m} & -0.57 \text{ ms}^{-1} & 0.055 \text{ ms}^{-1} \end{bmatrix}$.

The torques required to perform the P3 motion on the time interval $t \in [0, t_f]$ are depicted in Fig. 13. While the motion based on the AK stays within the limits, a following motion with the SK would be dynamically infeasible. The most significant difference is observed at the beginning of the following motion because here the desired velocity is the highest. In the second half, the dynamic requirements become smaller and stay within the constraints. This is owed to the fact that the desired relative acceleration results in a decreasing desired velocity. The dynamic requirements at the start of P3 are generally only met at very few points by the SK in our robot's workspace. The plot and frames in Fig. 14 illustrate how the AK exploit the virtual DOF to achieve dynamic feasibility. Further examples regarding virtual joint exploitation may be found in [36]. Fig. 15 shows
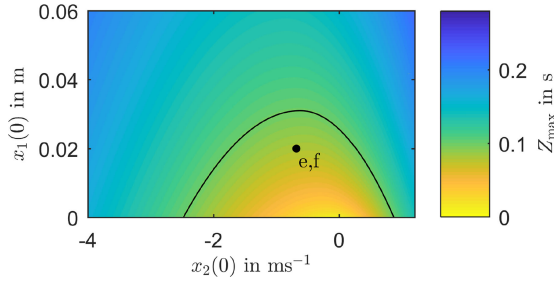
Fig. 15. Contours indicating the maximal Zeno time (27) for Example 3 acceleration bounds in P3 $\left(\gamma(t) \in [29.5, 49.5] \text{ ms}^{-2}\right)$ with the same scale as in Fig. 8, but doubled $\Delta\gamma$ for increased robustness. The solid contour marks $Z_{\max} = 0.101$ s in view of (29). A further result of the optimization compared to Fig. 8 is the reduction of the maximum occurring Zeno time from 0.28 s to 0.22 s in the depicted subspace.

the maximal Zeno time as described in Section IV-A, but here with the optimized solutions for γ and t_f from Example 3. In comparison to Fig. 8, the Zeno times with respect to the initial relative state have generally decreased.

D. Acceleration Planning for Throwing and Catching

In P1 and P2, cf., Fig. 2, the throwing and the catching robot accelerate from a resting position to a dynamic goal state. In P4, the catching robot decelerates from a dynamic state to a resting position. These three phases demand the solution of two-point boundary value problems of the same dynamical system (robot) with different nonlinear constraints. Our method of choice is the formulation of a constrained optimal control problem

$$\underset{\boldsymbol{\tau}}{\text{minimize}} \quad \frac{1}{2} \int \boldsymbol{\tau}^\top \boldsymbol{\tau} \, \mathrm{d}t$$

$$\text{s.t.} \quad (35), \ \boldsymbol{h}(\boldsymbol{q}, \dot{\boldsymbol{q}}, \boldsymbol{\tau}) \leq 0, \ h^{(1,4)}(t, \boldsymbol{q}, \dot{\boldsymbol{q}}, \boldsymbol{\tau}) \leq 0$$

$$\boldsymbol{h}_0(\boldsymbol{q}, \dot{\boldsymbol{q}}, t_0, t_f) = 0 \qquad (43)$$

that penalizes large absolute torques quadratically. This approach allows to account for the appearance of large rotational velocities that require operation close to the motor velocity limits or to the peak torque limits of the gears. Indicated by the different superscripts of $\boldsymbol{h}$, P1 and P4 require task-dependent nonlinear constraints, which are described in the following discussion.

For *throwing acceleration* (P1), the goal state of the robot is determined by the desired release state of the ball. As the throw is carried out without grasping, the relative acceleration in normal end-effector direction must always be negative in this phase. A way of calculating this relative normal acceleration is explained in [9] and contained in $h^{(1,4)}$. In order to fix the ball in tangential direction, we have advanced the end-effector design of the Shannon-juggler by Schaal and Atkeson [13] from the V-shape to the one depicted in Fig. 16. This design exploits centripetal forces during the rotational acceleration to fix a spherical object in a known position relative to the end-effector. Stopping at the release instant t_r is realized by resetting the desired joint velocities to zero. The desired joint angles are kept constant for
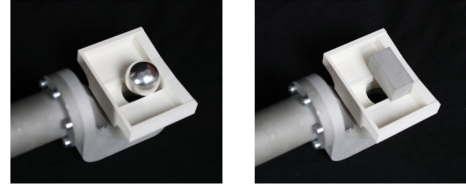

Fig. 16. End-effector design that reduces contact surface with the ball and thus avoids jamming. Spherical objects are automatically driven to the depicted throwing position, cuboids must be placed manually.
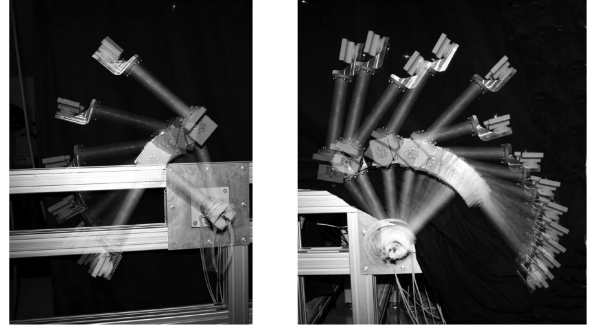

Fig. 17. Visualization of the throwing (left) and catching (right) motion.

$t \geq t_r$, respectively. The resulting throwing motion is visualized on the left in Fig. 17.

For *catching acceleration* (P2), the goal state of the robot is determined by the desired robot state at the beginning of the subsequent following motion (P3) based on the choice of the initial state in (17) using inverse kinematics from (37). Unlike for throwing, no normal acceleration constraint with respect to the end-effector applies for this phase.

For *catching deceleration* (P4), the initial state is the last state of the following motion, which does not change due to the offline computation of P3. The final state of this phase is the resting position from which the throwing motion starts accelerating in the next step. During this phase the relative acceleration in normal end-effector direction must be kept negative $(h^{(1,4)})$ to maintain stable bouncing and then continuous contact with the ball.

VI. EXPERIMENTS

Here, we introduce the experimental setup shown in Fig. 18. Then, several sets of experiments with a large amount of trials evaluate the effectiveness of the optimization based motion planner and to what extend the proposed methods allow prediction of success and failure. Moreover, repeatability beyond spherical objects is demonstrated using a cuboid. A video in the multimedia attachment provides slow motion scenes of the experiment.

A. Setup

Two 2-DOF robots that are symmetrically mounted in a vertical plane serve as the basis for the experiments. Fig. 18 visualizes the setup and Table I summarizes the robot's kinematic and dynamic parameters that are also used for the optimizations in the previous section. A simple high-gain PD-controller jointly

Fig. 18. Experimental setup with two symmetric robots acting in a common vertical plane. Each robot has two actuated rotational degrees of freedom and is capable of performing both the throwing and the catching task, without change of hardware.

TABLE III
EXPERIMENTAL SETS

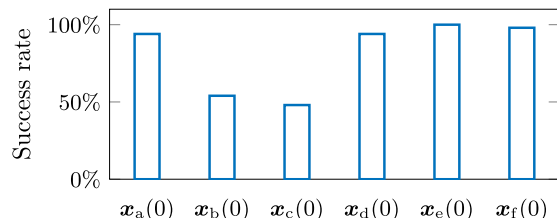| Symbol	$h(0)$	$\nu(0)$	Object	$h_{\max}$	Success
Unit	m	ms^{-1}	-	m	-
$\boldsymbol{x}_a(0)$	0.020	-0.46	Ball	0	75/80
$\boldsymbol{x}_b(0)$	0.035	-0.46	Ball	0	38/80
$\boldsymbol{x}_c(0)$	0.020	0	Ball	0	43/80
$\boldsymbol{x}_d(0)$	0.035	-0.46	Ball	0.005	75/80
$\boldsymbol{x}_e(0)$	0.020	-0.68	Ball	0	**80/80**
$\boldsymbol{x}_f(0)$	0.020	-0.68	Cuboid	0	78/80

Fig. 19. Successful trials out of 80 for each test set $\boldsymbol{x}_0^a - \boldsymbol{x}_0^f$ from Figs. 8, 11, and 15. See Table III for details.

operates both robots at 1 kHz. If we let the joint displacement error and joint velocity error be e and $\dot{e}$, respectively, the control law is $\boldsymbol{\tau} = K_P \boldsymbol{e} + K_D \dot{\boldsymbol{e}}$ with $K_P = 12000$ and $K_D = 100$. The joints consist of RE40 Maxon DC motors, MR Maxon (type L) 1024-bit encoders, and HFUC Harmonic Drive 1:100 gears. Hence, the joint displacement on the load side is measured with an accuracy of $1.5 \cdot 10^{-5}$ rad.

At the end of the kinematic chain, very simple, nonactuated, box-like end-effectors are mounted, which is the major difference in comparison to grasping-based catching. As a result of our simplistic setup, the timely interception of an object's flight trajectory (with appropriate gripper orientation) is not anymore sufficient for successful catching. Hence, a P3 catching motion will lead to (partial) failure, if the occurring uncertainties U1–U3 are not sufficiently compensated. For example, any static catching approach would result in a success rate of 0%.

Choosing the described robot–robot scenario also allows to exclude human throwers and complex vision systems as potential sources for failed catching attempts. Moreover, robotic throws are repeatable except for uncertainties, which can be assumed bounded. Given that no significant in-flight perturbations occur, we can then link experimental catching success with critical parameters discussed in theory and simulation beforehand, e.g., relative acceleration or initial relative states. With the robust choice of the critical parameters proposed in this paper, offline motion planning and open-loop operation become sufficient for successful catching.

Due to the robustness considerations derived in this paper, no visual feedback is needed during operation. Nonetheless, we must perform a nonrecurring calibration of the release angle α_r and velocity ν_r. The first reason is that in the nonprehensile throwing approach the ball does not leave the box immediately, but slides along the edge of the box for a short time. During sliding, the revolute joints perform a small angular overshoot, which depends on various parameters. However, even for a simple PD-controlled robot the error in the release angle α_r, here approximately $3°$, does not differ notably in-between trials. Second, the experimental setup is not perfectly symmetric, which requires a difference in the release velocity ν_r of 2% depending on the direction. The velocity is modified using standard dynamic trajectory scaling [37]. The remaining uncertainties and inaccuracies must be compensated by the robust catch.

B. Evaluation and Discussion

The experiment intends to validate the presented formalism in terms of catching success and dynamic feasibility. Moreover, we take advantage of the repeatability the robot–robot experiment provides in order to evaluate the robustness quantification from Section IV-A. Therefore, the six test sets $\boldsymbol{x}_{a-f}(0)$ listed in Table III are carried out based on the three realistic simulation examples used throughout the paper. As a reference, each test set is additionally marked in Figs. 8, 11, and 15, respectively. Calibration and throwing motion are the same for all trials and sets. The statistical results are depicted in Fig. 19, each based on 80 sequential trials per set, 40 in each direction. Slow motion examples of typical catches (success and failure) are provided with the media attachment.

The first three sets $\boldsymbol{x}_{a-c}(0)$ have not undergone the cost optimization (42) and are based on Example 1 using a low edge[8] box. Nonetheless, we used the implementation of (42) to find a dynamically feasible joint trajectory. Fig. 20 exemplarily illustrates the small errors. The initial relative velocity for the sets $\boldsymbol{x}_{a-b}(0)$ is chosen according to Corollary 2, whereas $\boldsymbol{x}_c(0)$ represents velocity matching, a common choice in literature. Comparing the good results of $\boldsymbol{x}_a(0)$ with the inferior results of $\boldsymbol{x}_c(0)$, the increased robustness through the use of Corollary 2 becomes apparent. Moreover, the robustness quantification (27)–(29) correctly predicts significantly worse performance for $\boldsymbol{x}_b(0)$ compared to $\boldsymbol{x}_a(0)$ as the maximal Zeno time of $\boldsymbol{x}_b(0)$ is longer than the P3 duration. Hence, the experiment underlines the suitability of (27)–(29) to determine the range of potentially successful initial relative states for particular catching motions. Nonetheless, even in the presented controlled environment, various uncertainty factors exist, which prevent exact predictions of success and failure.

Test set $\boldsymbol{x}_d(0)$ in comparison to set $\boldsymbol{x}_b(0)$ serves to validate Corollary 1 and therefore evaluate the influence of the box

---

[8]As low edge boxes we regard edge heights of less or equal than the distance between an object's center of mass and its farthermost point on $\mathcal{S}_O$.
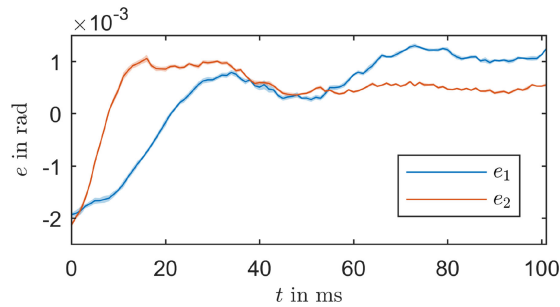
Fig. 20. Very small mean joint errors during P3 of ten $x_a(0)$-trials verify dynamic feasibility. The shaded areas indicate tree times the standard deviation. From these errors results a worst case Euclidean error in the workspace of less than 3 mm.
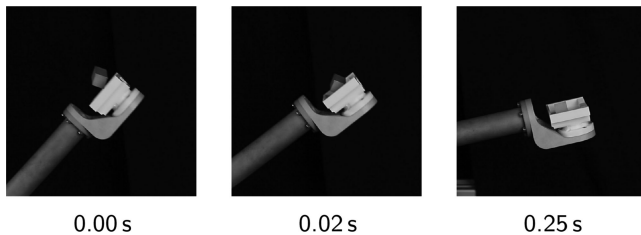

Fig. 21. Frames illustrating the successful catch of a cuboid.

height on the catching robustness. Noting that the initial relative state $x_d(0)$ fulfills (34) and not (29), the correctly predicted improvement supports the use of Corollary 1 to explore the effect of box height on catching success. Furthermore, the experiments validate a beneficial effect using the cost function (42), which originated in the proof of Theorem 1.

Test set $x_e(0)$ evaluates the optimized P3 motion as described in Example 3. In view of Corollary 2, the reduced initial relative velocity $\nu(0) = -0.68 \text{ ms}^{-1}$ accounts for the changes in γ, $\Delta\gamma$, and t_f. As can be seen from the results in Table III, the optimized solution improved the already good results from $x_a(0)$ to a sequence of 80 successful catches without failure. The improvements are mainly due to the increased relative acceleration. Hence, we may here infer that the presented approach sufficiently compensates for the occurring uncertainties U1–U3 in case of the ball object.

The cuboid depicted in Fig. 16 is used in set $x_f(0)$ to evaluate the potential generalizability for arbitrary object shapes. We, here use the same robot motions as in the previous set $x_e(0)$, which provides more robustness against the unpredictable collision effects than the data in Example 2. In contrast to the ball experiments, note that an operator relocates the cuboid after every catch to the throwing position shown in Fig. 16 as the end-effector design automates relocation only for spherical objects. The result are 78 successful catches, cf., Fig. 21, in a sequence of 80 using a low edge box. Due to these promising results, we believe that the Zeno-based approach constitutes a suitable basis for a more rigorous generalization in terms of arbitrary object shapes.

VII. Conclusion

In this paper, we presented a novel and provably robust framework for robotic catching of spherical objects. The achieved ro-

bustness allows for uncertainties at all planning stages, including but not limited to imprecise impact models and imprecise estimation of the object state. A particular emphasis is placed on the latter, which equals an uncertain initial state in our model. As a result, it could be shown in simulation and experiment that goal definitions in robotic catching with a particular negative initial relative velocity between the object and end-effector significantly increase the success rate.

Analyzing the robustness is made possible through parameterization of 3-D catching as a 1-D problem on the ballistic path. Therefore, we close the gap between robotic catching and the 1-D bouncing ball problem often considered in hybrid control theory. With the 1-D model, progress in hybrid control theory becomes accessible. A particular approach focusing on the Zeno behavior of bouncing balls, that is the occurrence of infinitely many impacts in a finite amount of time, is applied and extended. The 1-D solutions are then transformed back into 3-D while respecting all relevant kinematic and dynamic limitations. Considering these constraints prevents dynamically infeasible motions, which were declared a major reason for erroneous experiments in the past. The limitations could even be satisfied with 2-DOF robots because the nonprehensile task execution was exploited in form of a virtual prismatic joint.

The robustness with respect to the impact model has shown to be particularly beneficial for catching polygonal objects, which are known to suffer from the poor predictability of collision outcomes. Collisions of polygonal objects, however, transform normal relative velocity partially into tangential relative velocity, which was neglected in the process of parameterization. The neglected tangential relative motion influences the normal relative acceleration [9], which we analyze in simulation. Hence, the success claims are less precise for such objects or a larger range of relative acceleration must be considered at planning stage. Nonetheless, an experiment could show reliable catching for a cuboid.

Depending on the application, one may not only search for maximum success but also for minimum impact forces, minimum impact velocity, or a robot linkage optimized for the catching task. The 1-D model with the relative acceleration as input constitutes an easy and powerful tool to formulate such alternative goals. The presented methods may then be used to identify what hardware is necessary to achieve the goal, e.g., dynamical capabilities of the robot or object state accuracy. In order to achieve more accuracy or inter–trial flexibility, existing object tracking frameworks could be added and combined with a more flexible version of virtual joint motion planning [36]. As most promising, we expect the effect of accurate proximity sensing of h with high-temporal resolution because it would allow for closed-loop robotic catching.

References

[1] B. Bäuml, T. Wimböck, and G. Hirzinger, "Kinematically optimal catching a flying ball with a hand-arm-system," in *Proc. IEEE/RSJ Int. Conf. Intell. Robot. Syst.*, 2010, pp. 2592–2599.

[2] J. Kober, M. Glisson, and M. Mistry, "Playing catch and juggling with a humanoid robot," in *Proc. IEEE-RAS Int. Conf. Hum. Robot.*, 2012, pp. 875–881.

[3] V. Lippiello, F. Ruggiero, and B. Siciliano, "3D monocular robotic ball catching," *Robot. Auton. Syst.*, vol. 61, no. 12, pp. 1615–1625, 2013.

[4] S. Kim, A. Shukla, and A. Billard, "Catching objects in flight," *IEEE Trans. Robot.*, vol. 30, no. 5, pp. 1049–1065, Oct. 2014.

[5] B. Hove and J.-J. Slotine, "Experiments in robotic catching," in *Proc. IEEE Amer. Contr. Conf.*, 1991, pp. 380–386.

[6] W. Hong and J.-J. E. Slotine, "Experiments in hand-eye coordination using active vision," in *Exp. Robotics IV*, ser. Lecture Notes in Control and Information Sciences. London, U.K.: Springer, 1997, vol. 223, pp. 130–139.

[7] M. Buehler, D. E. Koditschek, and P. J. Kindlmann, "Planning and control of robotic juggling and catching tasks," *Int. J. Robot. Res.*, vol. 13, no. 2, pp. 101–118, 1994.

[8] G. Bätz, A. Yaqub, H. Wu, K. Kühnlenz, D. Wollherr, and M. Buss, "Dynamic manipulation: Nonprehensile ball catching," in *Proc. Mediterranean Conf. Control Automat.*, 2010, pp. 365–370.

[9] M. M. Schill, F. Gruber, and M. Buss, "Quasi-direct nonprehensile catching with uncertain object states," in *Proc. IEEE Int. Conf. Robot. Autom.*, 2015, pp. 2468–2474.

[10] S. S. M. Salehian, M. Khoramshahi, and A. Billard, "A dynamical system approach for softly catching a flying object: Theory and experiment," *IEEE Trans. Robot.*, vol. 32, no. 2, pp. 462–471, Apr. 2016.

[11] K. M. Lynch and M. T. Mason, "Dynamic nonprehensile manipulation: Controllability, planning, and experiments," *Int. J. Robot. Res.*, vol. 18, no. 1, pp. 64–92, 1999.

[12] F. Ruggiero, V. Lippiello, and B. Siciliano, "Nonprehensile dynamic manipulation: A survey," *IEEE Robot. Autom. Lett.*, vol. 3, no. 3, pp. 1711–1718, Jul. 2018.

[13] S. Schaal and C. G. Atkeson, "Open loop stable control strategies for robot juggling," in *Proc. IEEE Int. Conf. Robot. Autom.*, 1993, pp. 913–918.

[14] A. Pekarovskiy, F. Stockmann, M. Okada, and M. Buss, "Hierarchical robustness approach for nonprehensile catching of rigid objects," in *Proc. IEEE/RSJ Int. Conf. Intell. Robot. Syst.*, 2014, pp. 3649–3654.

[15] R. Ronsse, P. Lefevre, and R. Sepulchre, "Sensorless stabilization of bounce juggling," *IEEE Trans. Robot.*, vol. 22, no. 1, pp. 147–159, Feb. 2006.

[16] P. Reist and R. D'Andrea, "Design and analysis of a blind juggling robot," *IEEE Trans. Robot.*, vol. 28, no. 6, pp. 1228–1243, Dec. 2012.

[17] A. A. Rizzi and D. E. Koditschek, "Further progress in robot juggling: the spatial two-juggle," in *Proc. IEEE Int. Conf. Robot. Autom.*, 1993, pp. 919–924.

[18] T. L. Vincent, "Controlling a ball to bounce at a fixed height," in *Proc. IEEE Amer. Contr. Conf.*, 1995, pp. 842–846.

[19] S. Schaal, C. G. Atkeson, and D. Sternad, "One-handed juggling: A dynamical approach to a rhythmic movement task," *J. Motor Behav.*, vol. 28, no. 2, pp. 165–183, 1996.

[20] A. Zavala-Rio and B. Brogliato, "On the control of a one degree-of-freedom juggling robot," *Dyn. Control*, vol. 9, no. 1, pp. 67–90, 1999.

[21] B. Brogliato, *Nonsmooth Mechanics: Models, Dynamics, and Control*, 2nd ed., (ser. Communications and control engineering). New York, NY, USA: Springer, 1999.

[22] R. Ronsse, P. Lefevre, and R. Sepulchre, "Rhythmic feedback control of a blind planar juggler," *IEEE Trans. Robot.*, vol. 23, no. 4, pp. 790–802, Aug. 2007.

[23] R. G. Sanfelice, A. R. Teel, and R. Sepulchre, "A hybrid systems approach to trajectory tracking control for juggling systems," in *Proc. IEEE Conf. Dec. Contr.*, 2007, pp. 5282–5287.

[24] J. J. BenjaminBiemond, N. van de Wouw, Heemels, W. P. Maurice H. Heemels, and H. Nijmeijer, "Tracking control for hybrid systems with state-triggered jumps," *IEEE Trans. Automat. Contr.*, vol. 58, no. 4, pp. 876–890, Apr. 2013.

[25] A. Saccon, N. van de Wouw, and H. Nijmeijer, "Sensitivity analysis of hybrid systems with state jumps with application to trajectory tracking," in *Proc. IEEE Conf. Dec. Contr.*, 2014, pp. 3065–3070.

[26] R. Goebel, R. G. Sanfelice, and A. Teel, "Hybrid dynamical systems," *IEEE Contr. Syst.*, vol. 29, no. 2, pp. 28–93, Apr. 2009.

[27] K. M. Lynch and T. D. Murphey, "Control of nonprehensile manipulation," in *Control Problems in Robotics*, (ser. Springer Tracts in Advanced Robotics.) New York, NY, USA: Springer, 2003, vol. 4, pp. 39–57.

[28] J. Zhang, K. H. Johansson, J. Lygeros, and S. Sastry, "Zeno hybrid systems," *Int. J. Robust Nonl. Contr.*, vol. 11, no. 5, pp. 435–451, 2001.

[29] M. K. Camlibel and J. M. Schumacher, "On the zeno behavior of linear complementarity systems," in *Proc. IEEE Conf. Dec. Contr.*, 2001, pp. 346–351.

[30] M. Heymann, FengLin, G. Meyer, and S. Resmerita, "Analysis of zeno behaviors in a class of hybrid systems," *IEEE Trans. Automat. Contr.*, vol. 50, no. 3, pp. 376–383, Mar. 2005.

[31] A. D. Ames and S. Sastry, "On the stability of zeno equilibria," in *Proc. 9th Int. Workshop Hybrid Syst. Comput. Control*. Berlin, Germany: Springer, 2006, pp. 34–48.

[32] R. Goebel and A. R. Teel, "Lyapunov characterization of zeno behavior in hybrid systems," in *Proc. IEEE Conf. Dec. Contr.*, 2008, pp. 2752–2757.

[33] Y. Or and A. D. Ames, "Stability and completion of zeno equilibria in lagrangian hybrid systems," *IEEE Trans. Automat. Contr.*, vol. 56, no. 6, pp. 1322–1336, Jun. 2011.

[34] A. Lamperski and A. D. Ames, "On the existence of zeno behavior in hybrid systems with non-isolated zeno equilibria," in *Proc. IEEE Conf. Dec. Contr.*, 2008, pp. 2776–2781.

[35] Y. Or and A. R. Teel, "Zeno stability of the set-valued bouncing ball," *IEEE Trans. Automat. Contr.*, vol. 56, no. 2, pp. 447–452, Feb. 2011.

[36] M. M. Schill and M. Buss, "Kinematic trajectory planning for dynamically unconstrained nonprehensile joints," *IEEE Robot. Autom. Lett.*, vol. 3, no. 2, pp. 728–734, Apr. 2018.

[37] J. M. Hollerbach, "Dynamic scaling of manipulator trajectories," *J. Dyn. Sys. Meas. Contr.*, vol. 106, no. 1, pp. 102–106, 1984.

Markus M. Schill received the Bachelor's degree and the Diploma Engineer degree in electrical engineering from the Department of Electrical Engineering and Information Technology, Technical University of Munich, Munich, Germany, in 2010 and 2012, respectively. He is currently working toward the Ph.D. degree in hybrid system stabilization and robot motion planning for robust manipulation from the Chair of Automatic Control Engineering, Department of Electrical and Computer Engineering, Technical University of Munich, Germany.

Since 2013, he has been a Researcher with the Chair of Automatic Control Engineering, Department of Electrical and Computer Engineering, Technical University of Munich, Germany. His research interests include the area of automatic control and robotics with a focus on hybrid systems and optimal motion planning.

Martin Buss received the Diploma Engineer degree in electrical engineering from the Technical University Darmstadt, Darmstadt, Germany, in 1990 and the Doctor of Engineering degree in electrical engineering from University of Tokyo, Tokyo, Japan, in 1994. He received the Habilitation degree from the Department of Electrical Engineering and Information Technology, Technical University of Munich, Munich, Germany, in 2000.

In 1988, he was a Research Student with the Science University of Tokyo, Japan, for one year. As a Postdoctoral Researcher, he stayed with the Department of Systems Engineering, Australian National University, Canberra, ACT, Australia, from 1994 to 1995. From 1995 to 2000, he was a Senior Research Assistant and Lecturer with the Institute of Automatic Control Engineering, Department of Electrical Engineering and Information Technology, Technical University of Munich, Germany. He has been appointed as a Full Professor, the Head of the Control Systems Group and the Deputy Director of the Institute of Energy and Automation Technology, Faculty IV–Electrical Engineering and Computer Science, Technical University Berlin, Berlin, Germany, from 2000 to 2003. Since 2003, he has been a full Professor (Chair) with the Chair of Automatic Control Engineering, Technical University of Munich, Germany. From 2006 to 2014, he was the Coordinator of the DFG Excellence Research Cluster Cognition for Technical Systems CoTeSys.

Dr. Buss has been awarded the ERC Advanced Grant SHRINE.